

Performance of PEFC under Different Gas-mixing Conditions

Yulei Ma, Miho Kageyama, and Motoaki Kawase

Department of Chemical Engineering, Kyoto University, Kyotodaigaku-Katsura,
Nishikyo-Ku, Kyoto 615-8510 Japan

For PEFCs' grand-scale commercialization, their performance should be further improved. The performance of PEFC is the results of the distribution of local current density and materials concentration, especially oxygen and water. In addition, the in-plane transport of reactant gas in the gas diffusion layer (GDL), which is difficult to measure, affects the distribution of oxygen partial pressure and relative humidity (RH) by mixing the gas with different residence time. In this study, the distribution of local current density as well as oxygen partial pressure and RH was estimated by varying active area and gas flow rate. Furthermore, two kinds of different gas channels, parallel and serpentine, were utilized to estimate the effect of gas mixing in the GDL. The concept of space time was used to discuss the effects of gas mixing in the perspective of chemical engineering. The results may provide a theory basis for a cell design procedure.

Introduction

Polymer electrolyte fuel cells (PEFC) offer zero-emission energy conversion. However, for PEFCs' grand-scale commercialization, their performance should be further improved. The performance of PEFC is determined by the local current density or the oxygen reduction reaction (ORR) rate. Extensive studies have been carried out on explorations of the effect of factors such as temperature (1), total pressure (2), oxygen partial pressure (3), relative humidity (RH) (4) on the ORR rate as well as mass transfer rate. However, these parameters have distributions even in a single cell, and they may be dependent on each other, so that the effects of a single factor in the cell are complicated and uneasy to be clarified.

The ORR in PEFC is an exothermal reaction, so that the temperature profile exists in a cell in the through-plane and in-plane directions. The temperature at cathode catalyst layer surface is 1–2 °C higher than the temperature at gas channel, when the current density is 0.8 A/cm² and the cell temperature is 80 °C (5,6). On the other hand, the temperature distribution in the in-plane direction is more ununiform than that in the through-plane direction. The difference of the highest and lowest temperature in the electrode was less than 10 °C at 0.8 A/cm² in a cell with 50 mm × 50 mm active area observed by thermograph (7).

The total pressure also has a distribution in a cell due to the pressure drop along the gas channel. The pressure drop of the cell with 14.4 cm² active area and serpentine gas channel, whose depth, width, and total length are 1.0 mm, 1.0 mm and about 700.0 mm, is about 0.3 kPa, fed with 200 mL/min of N₂ at room temperature under atmospheric pressure (8).

The partial pressure profile of oxygen and water vapor affect the ORR rate distribution. On the other hand, the ORR can change the composition of the reactant gas, i.e. the molar fraction of oxygen and water vapor, so that the performance can also be affected by reactant conversion (9). Furthermore, gas flow pattern distributes the reactant gas in the in-plane direction, which also affect the cell performance (10). Since the pressure gradients and concentration gradients exist in the porous gas diffusion layer (GDL), the reactant gas can cross to the neighboring channels and the gas with different compositions are mixed, so that the gas composition distribution is also affected by the cross-flow phenomenon (11).

The distributions of properties, especially gas composition inside the cell, are difficult to be measured precisely without expensive equipment and high experimental techniques. Technologies such as gas chromatograph and laser absorption spectroscopy can be used to analyze the gas composition inside the cell (12). However, these ex-situ characterizations only yield the effective properties of the whole layer and do not resolve the local impact of morphological heterogeneity (13). By inserting an oxygen sensor, such as optical fiber covered by oxygen-sensitive dye film (14), microelectrochemical cell (15), into a specific location in a cell, the oxygen partial pressure can be measured *in-situ*. Micro-gas-chromatograph and tunable diode laser absorption spectroscopy techniques can be utilized to measure the water vapor partial pressure *in-situ* (12). Additionally, liquid water distribution can be measured by neutron and X-ray imaging (16,17).

The cell performance can be analyzed and predicted by numerical methods, which have been discussed extensively in the literature. Although many 3-dimensional, non-isothermal, multi-phase models have been reported (18, 19), most of the models are complicated with heavy computation load, and difficult to separate the effects of fluid dynamic, heat transfer, proton/electron transfer and electrochemical phenomenon. A computationally inexpensive method to summarize and understand the distributions of properties in the cell is lack of reporting. To clarify the effects of gas composition inside the cell, the concept of gas mixing and residence time distribution (RTD) in the perspective of chemical reaction engineering can be helpful.

The objective of this study is to demonstrate a method to evaluate the gas mixing property of gas channels, and to predict the cell performance. The RTD can be simulated by numerical method, so that the macromixing of gas with different space times can be evaluated. By regarding the PEFC as a reactor, the cell performance can also be predicted according to the reactor model which has similar RTD as the simulation results.

In addition, the cell performance under different space time conditions can be measured experimentally by changing the active area and gas flow rate, so that the gas composition profile can also be evaluated. The results are expected to provide a methodology to understand the gas macromixing in different shape of gas channels, and may be helpful for the cell design.

Numerical Calculation

In this study, a 3-dimensional computational fluid dynamics (CFD) model was developed to simulate the velocity and pressure fields in the cathode gas channels and GDLs. To get the RTD of the gas channel, a kind of tracer which is a stepwise change

in a special physical property, e.g., concentration, electrical conductivity, temperature, was supplied to the gas inlet continuously. Then the step responses at the gas channel outlet were simulated by solving time-dependent advection equations of the specific physical property. The calculation was achieved by finite volume method by using an open source toolbox OpenFOAM 8.

Model geometry

The geometries and meshes applied for parallel and serpentine channels in the calculation are shown in Figure 1. The gas flows from the inlets to the outlets, through the GDLs which were implemented as porous medias. The width and depth of gas channels are 1 mm, and the width of the ribs between the channels was 1 mm. The size of the GDLs were 22 mm in X direction, 21 mm in Y direction, and 0.190 mm in Z direction. The meshes of manifolds in parallel channels, bended part in serpentine channels, and GDLs were denser than that in other parts. The total number of cells applied in simulation was 383 000 for parallel gas channel and 373 000 for serpentine gas channels.

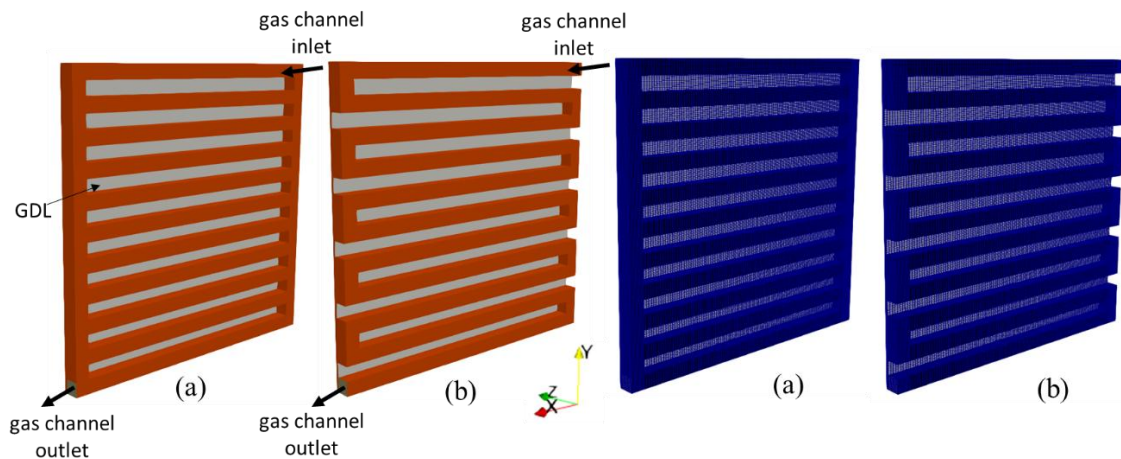


Figure 1. Geometries (left) and meshes (right) of flow fields ((a) parallel, (b) serpentine)

Assumptions

Steady state was assumed. The gas flow was incompressible laminar due to low velocities. Isotropic and homogeneous ideal gas which has uniform temperature, density, and viscosity was assumed. The GDL was regarded as a uniform porous medium. No liquid water condensed in the gas channel.

The tracer which has negligibly small diffusivity in the reactant gas was assumed. In another word, the convection of the tracer is great enough so that the diffusion of the tracer can be ignored.

CFD simulation

Governing equations applied to calculate the velocity and pressure fields are expressed by Eqs. [1] and [2]

Mass conservation:

$$\nabla \cdot (\rho \mathbf{U}) = 0 \quad [1]$$

Momentum conservation:

$$\nabla \cdot (\rho \mathbf{U} \mathbf{U}) - \nabla \cdot (\mu \nabla \mathbf{U}) = -\nabla P + \mathbf{S}_m \quad [2]$$

where \mathbf{U} represents the velocity vector, ρ and μ represent the density and viscosity of the reactant gas respectively. P is the total pressure, and \mathbf{S}_m is the momentum source term, which equals 0 in the gas channels and satisfies the Darcy's law in the GDLs given by Eq. [3].

$$\mathbf{S}_m = -\frac{\mu}{K} \mathbf{U} \quad [3]$$

The operating conditions and physical constants are listed in Table 1. The inlet Re number is 127 so that the gas flow can be regarded as laminar.

Table 1. Operating conditions and physical constants (353 K)

| Variable | Symbol | Value |
|---|----------------|--|
| Total pressure at gas channel outlet | P_L | 101325 Pa |
| Cell temperature | T | 353 K |
| Velocity at gas channel inlet | $ \mathbf{U} $ | 2.6658 m s ⁻¹ |
| Inlet molar fraction of O ₂ | y_{O_2} | 0.7532 |
| Inlet molar fraction of H ₂ O | y_{H_2O} | 0.2468 |
| Density | ρ | 0.9850 kg m ⁻³ |
| Viscosity | μ | 2.0675 × 10 ⁻⁵ Pa s (20,21) |
| Permeability of GDL (in-plane direction) | K_x, K_y | 1.30 × 10 ⁻¹¹ m ² (22) |
| Permeability of GDL (through-plane direction) | K_z | 8.99 × 10 ⁻¹² m ² (22) |

RTD simulation

The transport equation of the tracer is given by Eq. [4].

$$\frac{\partial \varphi}{\partial t} + \nabla \cdot (\varphi \mathbf{U}) - \nabla \cdot (\Gamma \nabla \varphi) = S_\varphi \quad [4]$$

where φ represents the specific physical property of the tracer, Γ represents the diffusivity of property, and S_φ represents the source term. \mathbf{U} is the velocity field calculated by CFD simulation mentioned above.

For example, when the φ represents the temperature, the Γ represents the heat diffusivity. In this study, Γ and S_φ equal 0, so that the Eq [4] can be simplified to a time-dependent advection equation, which means when the φ represents the temperature, the thermal conductivity is 0, and the heat can only be transferred by convection.

When setting the φ equals 1 at the vessel inlet and 0 in the whole vessel from the start time, the tracer is carried in the flow field until it fulfills the whole vessel. Then

by monitoring the φ at the vessel outlet, the time variation can be described as a cumulative RTD function, $F(t)$.

$$F(t) = \bar{\varphi}_L(t)/\bar{\varphi}_0(0) \quad [5]$$

where $\bar{\varphi}$ represents the integrated average value at inlet or outlet face, the arguments 0 and L represent the gas channel inlet and outlet, respectively. And the RTD function $E(t)$ and the mean residence time \bar{t} can be obtained by Eqs. [6] and [7].

$$E(t) = \frac{d}{dt} F(t) \quad [6]$$

$$\bar{t} = \int_0^{\infty} tE(t)dt \quad [7]$$

Reactor design equations

The ORR kinetics can be expressed as Eq. [8].

$$-r_{SO} = k_{gc}p_O \quad [8]$$

where p_O is the local oxygen partial pressure [Pa], and $-r_{SO}$ is the oxygen consumption rate per active area [mol/(m²s)], which was experimentally proved to be 1st-order to the oxygen partial pressure (23). k_{gc} represents the partial-pressure-based apparent kinetics constant [mol/(Pa·m²·s)] which is the function of cathode electromotive force and RH at a fixed temperature (24).

By assuming the kinetics constant k_{gc} is linear to the activity of the water vapor a_w which is equal to RH, and the water permeation flux through the membrane is 0, the oxygen partial pressure and the activity of the water vapor can be calculated from the oxygen conversion x_O by Eqs. [9] and [10], according to the material balance.

$$p_O = \frac{Py_{O0}(1 - x_O)}{1 + y_{O0}x_O} \quad [9]$$

$$a_w = \frac{P}{p_S^{\text{sat}}} \frac{y_{S0} + 2y_{O0}x_O}{1 + y_{O0}x_O} \quad [10]$$

where y_{S0} and y_{O0} represents the water vapor and oxygen molar fraction of the inlet gas, p_S^{sat} represents the saturated water vapor pressure at the cell temperature, P is the total pressure in the gas channel.

When the GDL is thick enough, the continuous oxygen partial pressure and RH distribution on the CL surface can be assumed independent on the location under gas channels and ribs. Therefore, the PEFC can be regarded as a continuous reactor, which has the gas-mixing behavior between plug flow reactor (PFR) and perfectly mixed flow reactor (CSTR), whose design equations can be written as Eqs. [11] and [12].

$$-r_{SO}d(A/v_0) = C_{O0}dx_O \quad [11]$$

$$-r_{SO}(A/v_0) = C_{O0}x_O \quad [12]$$

where A is the active area from the gas inlet [m^2], v_0 is the inlet gas volumetric flow rate [m^3/s], C_{O_0} is the oxygen concentration in the inlet gas [mol/m^3], and x_0 is the oxygen conversion. A/v_0 can be regarded as the space time of the reactant gas in the cell. By solving the Eqs. [8], [9], [10] and the design equation, the distributions of oxygen conversion, as well as the oxygen partial pressure and RH, can be estimated.

Experimental

A Japan Automobile Research Institute (JARI) type cell was used in the experiments. The active area was reduced to $2.0 \text{ cm} \times 2.0 \text{ cm}$ so that the temperature distribution is less ununiform in the in-plane direction. Two kinds of gas channels, i.e. parallel and serpentine, were used in the cell. The width and depth of gas channels are 1 mm, and the width of the ribs between the channels was 1 mm. The membrane electrode assembly (MEA) was consisted of the catalyst layers made of 50 wt% Pt/carbon black catalyst particles with ionomer and the membrane (Chemours NR-212). Ionomer/carbon weight ratio was 1.0, and the catalyst layers (CL) thicknesses of anode and cathode were $10 \mu\text{m}$. Carbon paper (Toray TGP-H-060) without microporous layer (MPL) was used as GDL.

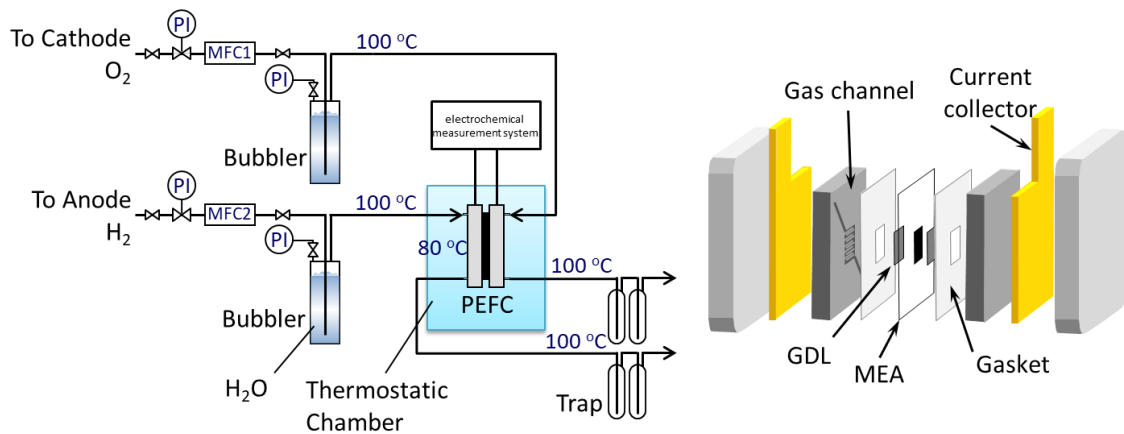


Figure 2. Experiment apparatus and cell structure

The MEAs with the same thickness and catalyst of CL were used in the experiment. On the other hand, the gaskets made of PTFE, which can block the mass transfer and electron conduction, had different opening area to obtain different active areas. The sizes of the gaskets opening were $2.0 \text{ cm} \times 2.0 \text{ cm}$, $2.0 \text{ cm} \times 1.5 \text{ cm}$, $2.0 \text{ cm} \times 1.0 \text{ cm}$, and the GDLs which had the same size of the gaskets opening were utilized in each experiment, as shown in Figure 3. Since the small active areas were applied, the distributions of the temperature and the total pressure in the gas channels were neglected.

The cell was operated in a thermostatic chamber whose temperature was controlled to maintain the temperature at the center of the cathode gas channel at $80 \text{ }^\circ\text{C}$. The pressure at the cell outlet was 1 atm. Pure H_2 and O_2 were humidified in bubblers at $65\text{--}75 \text{ }^\circ\text{C}$. H_2 flow rate was $60\text{--}200 \text{ cm}^3/\text{min}$ ($20 \text{ }^\circ\text{C}$, 1 atm) on dry basis. The stoichiometry of H_2/O_2 was 2.

Polarization curves and electrochemical impedance spectra were obtained using an electrochemical measurement system (Hokuto Denko Corp., HZ-7000). The

polarization curves were obtained by measuring the current at each cell voltage (0.005 V – OCV). The impedance spectra were measured in a range of frequency from 100 mHz to 100 kHz. A standard equivalent circuit model was employed to determine the high frequency resistance (HFR) (25). The cell voltage was corrected by the HFR results.

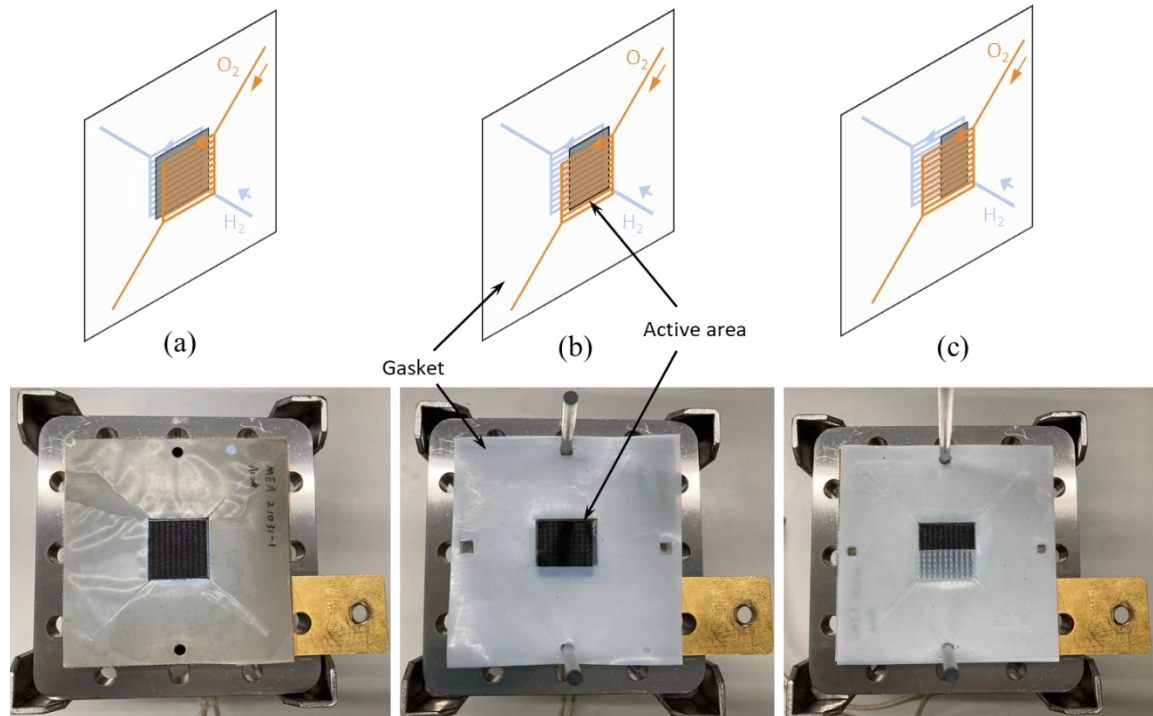


Figure 3. Different active areas utilized in the experiments ((a) 2.0 cm×2.0 cm, (b) 2.0 cm×1.5 cm, (c) 2.0 cm×1.0 cm)

Results and Discussion

Numerical calculation results

The velocity and pressure distributions of parallel and serpentine gas channels simulated by OpenFOAM 8 are shown in Figure 4. As shown in the velocity field in the gas channels ($z = 0.5$ mm), since the gas flow is separated into several channels in case of parallel channels, the gas velocity in each channel is much lower than that in 1-serpentine channel, and the pressure gradient of the serpentine channel is much higher than that of parallel channel. As a result, a large amount of gas flows across the rib to the neighbor channel in case of the serpentine channel, especially away from the bended parts where the neighbor gas channels are connected, and nearly no cross-flow gas was found in case of parallel channel as shown in the velocity field in the GDL ($z = 1.095$ mm).

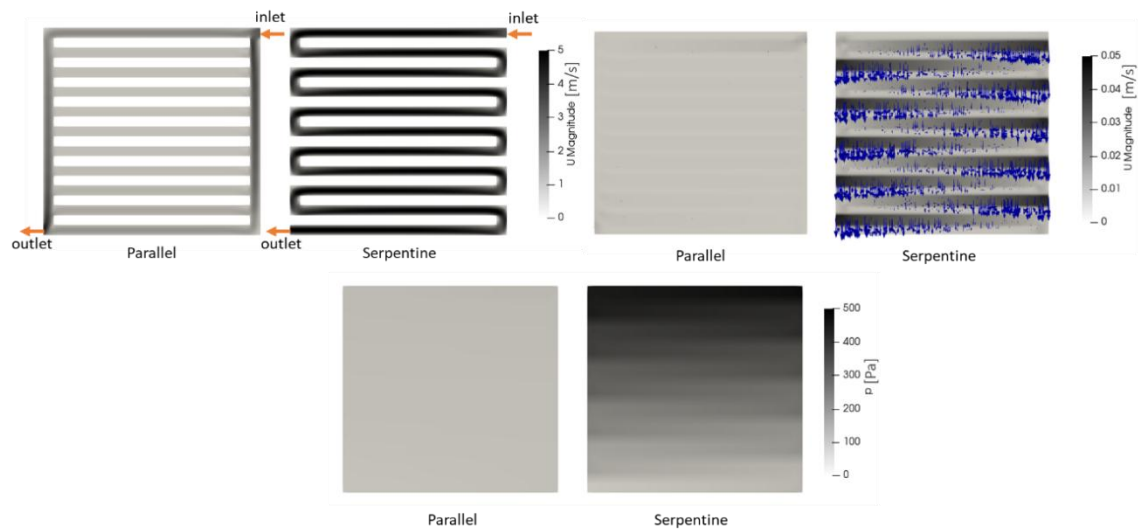
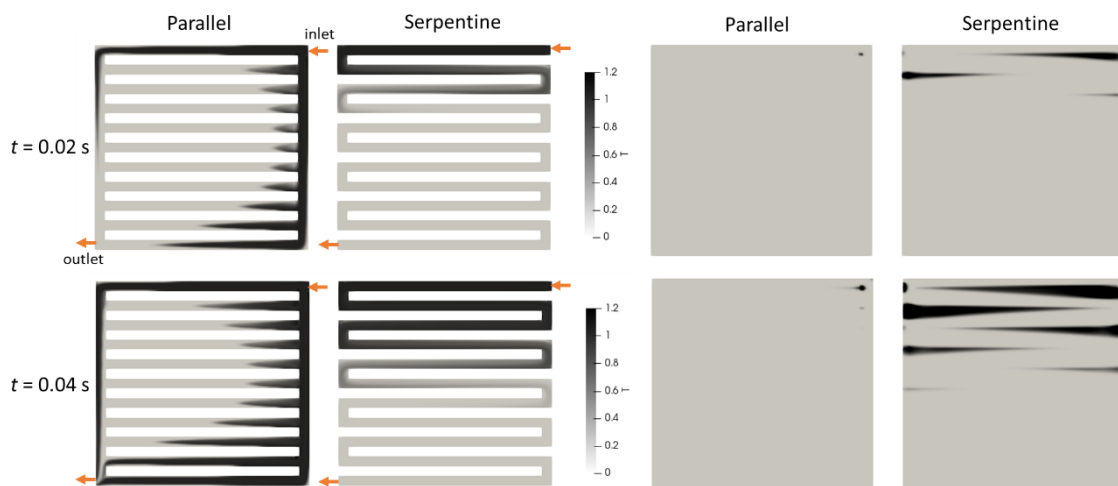


Figure 4. Velocity and pressure field in the center sections of gas channels and GDLs (top left: velocity at $z = 0.5$ mm, top right: velocity at $z = 1.095$ mm, bottom: gauge pressure at $z = 1.0$ mm)

Figure 5 shows the distribution of the property of the tracer, changing over time after starting the continuous feed of the tracer to the inlet. In case of the parallel channel, the property convection rate in the channels near the inlet and outlet is 2–4 times higher than that in the medium channels, due to the nonuniform velocity distribution. Since a part of the gas flows to the outlet quickly, the tracer can be detected earlier than the case of serpentine. After 1 second from feeding the tracer, it nearly fulfilled the whole gas channel, and the concentration in the GDL of parallel channel is still much lower than that of the serpentine channel, which also indicates the cross-flow in GDL under the parallel channel is much weaker than that of the serpentine channel.



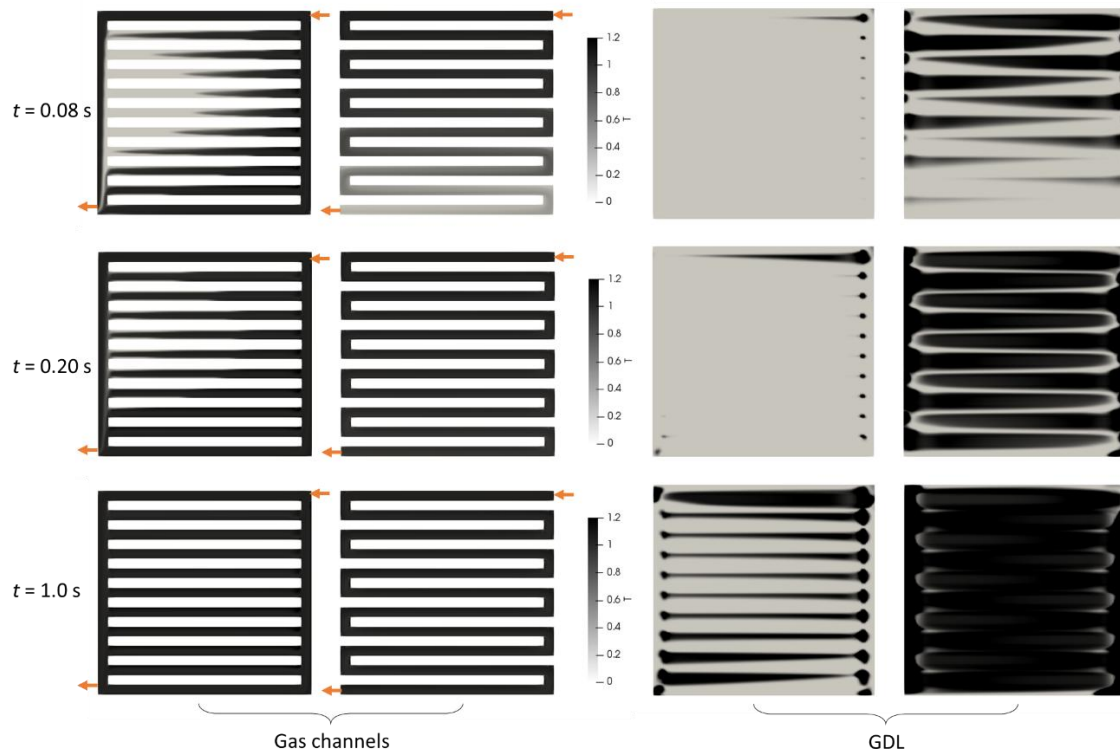


Figure 5. Time variation of the property of the tracer in the center sections of gas channels and GDLs (left: $z = 0.5$ mm, right: $z = 1.095$ mm)

By analyzing the time variation of integrated average property of the tracer in the outlet faces, the RTD can be obtained, as shown in Figure 6. The mean residence time, variance and skewness are also shown in Figure 6. The mean residence time of parallel is shorter than the serpentine channel, which indicates some dead volume may exist in the GDL in case of parallel channel. Some oscillation of RTD function of the parallel channels can be detected, due to the nonuniform distribution of the velocity.

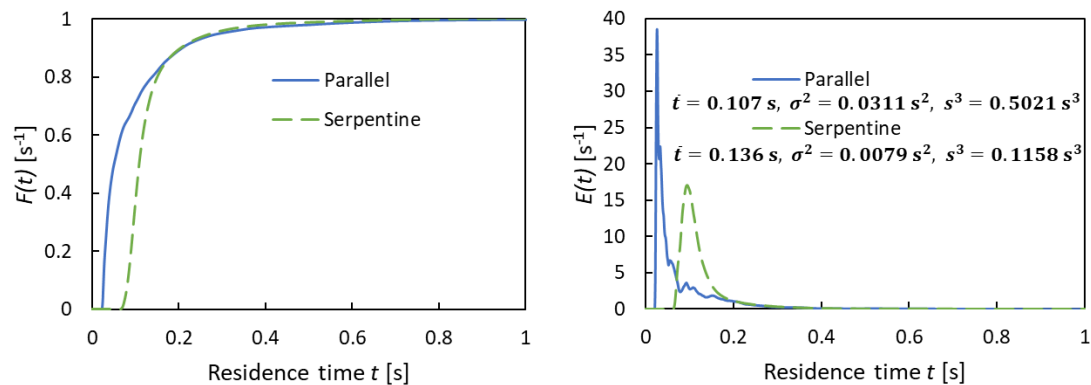


Figure 6. Residence time distribution of parallel and serpentine channels

By normalizing the residence time by the mean residence time, the RTD functions of dimensionless residence time can be derived, as shown in Figure 7. The RTD functions of CSTR, PFR and laminar flow reactor (LFR) plotted in Figure 7 were calculated by equations listed in Table 2.

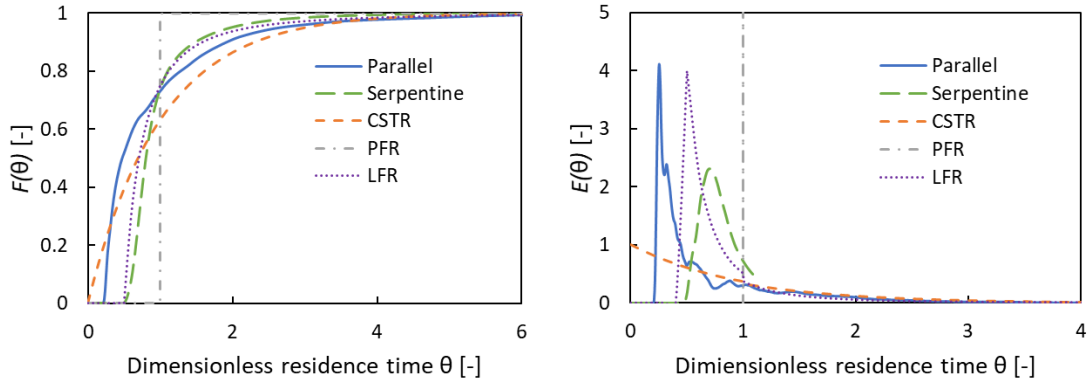


Figure 7. Dimensionless-residence-time distributions of different channels and models

Table 2. Dimensionless-residence-time-based RTD function of different model ($\theta = t/\bar{t}$)

| Model | $F(\theta)$ | $E(\theta)$ |
|-------|--|--|
| CSTR | $1 - \exp(-\theta)$ | $\exp(-\theta)$ |
| PFR | $U(\theta - 1)$ (Step function) | $\delta(\theta - 1)$ (Dirac delta function) |
| LFR | $\begin{cases} 0 & (0 \leq \theta < 0.5) \\ 1 - 1/(4\theta^2) & (\theta \geq 0.5) \end{cases}$ | $\begin{cases} 0 & (0 \leq \theta < 0.5) \\ 1/(2\theta^3) & (\theta \geq 0.5) \end{cases}$ |

The response of the parallel channels is similar to PFR for the short residence time components and CSTR for the long residence time components. The mixing of the gas near the inlet of the parallel gas channels is not obvious, since the pressure gradient between neighbor gas channels is gentle. On the other hand, the gas mixes near the outlet of the parallel gas channels. Consequently, the PFR followed by CSTR model can be considered to simulate the performance with parallel channels, shown as Figure 8.

On the other hand, in case of serpentine channels, the gas near the inlet is mixed with the gas in the neighbor channels, and then flows like in PFR, since the cross-flow is remarkable near the gas inlet and weak near the bended parts. Therefore, the CSTR followed by PFR model can be considered to simulate the performance with serpentine channels. More accurate model such as CSTR followed by PFR in several parallel line can also be considered. Both of the PFR followed by the CSTR and CSTR followed by PFR has the same RTD function which can be written as Eq. [13].

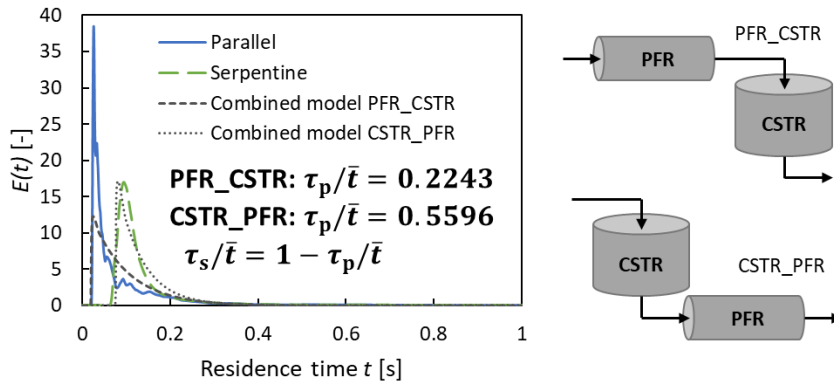


Figure 8. The RTD functions of parallel gas channels and compartment model

$$E(t) = \begin{cases} 0 & (t < \tau_p) \\ \frac{\exp\left(-\frac{t - \tau_p}{\tau_s}\right)}{\tau_s} & (t \geq \tau_p) \end{cases} \quad [13]$$

where \bar{t} is the mean residence time, τ_p and τ_s are the space time of PFR and the space time of CSTR. The macromixing in the gas channel and GDL can be represented by these two space times, τ_p and τ_s . The serpentine channel exhibited $\tau_p/\bar{t} = 0.56$ which is closer to the plug flow than the parallel flow exhibiting $\tau_p/\bar{t} = 0.22$.

Experimental results

Figure 9 shows the experimental polarization curves of different active areas and inlet gas flow rates in case of parallel gas channels, where the cell voltages are corrected by experimental HFR results. In case of large active area, higher current density was observed under high cell voltage, which resulted from the relatively high average RH of gas due to humidification by the water produced in ORR, and the decrease of oxygen partial pressure is little which cannot overtake the effects of the humidification. It infers that the ORR has the similar behavior of the self-catalytic reaction. The humidification of the water increases the ORR rate at low oxygen conversion, on the other hand, the decreasing oxygen partial pressure reduces the ORR rate at high conversion.

However, the limited current density is higher in case of the 2 cm×1 cm, and limited current densities in cases of the 2 cm×1.5 cm and 2 cm×2 cm are nearly equal. The reason may be the flooding occurs in case of the larger active area, so that the oxygen transfer resistance increases due to the presence of liquid water. On the other hand, the difference in limited current density between 2 cm×1 cm and other cases is smaller in case of gas flow rate of 2.69 mL/s, comparing to 1.35 mL/s, which infers that the humidification of the produced water is less effective in case of the high gas flow rate, so that the flooding is less remarkable. The results also indicate that the flooding occurs at the 1/2–3/4 length of the gas channel from the inlet.

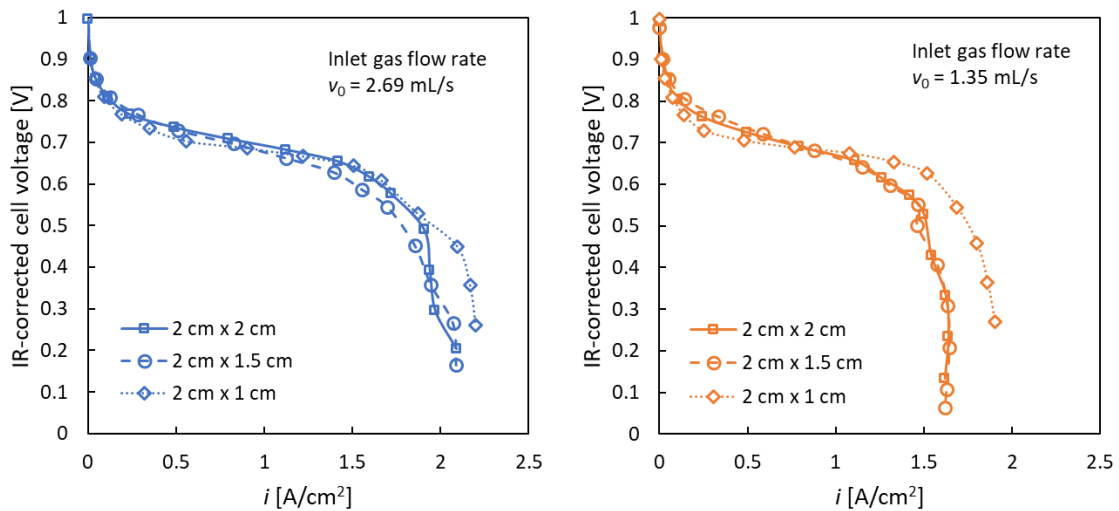


Figure 9. Polarization curves of different active areas (parallel gas channel)

Figure 10 shows the polarization curves of different inlet gas flow rates in the fixed active area in case of the parallel gas channels. The performances are the same when the current density is lower than 0.6 A/cm², which indicates that the effect of the water humidification compensated the effects of the oxygen consumption. However, the limited current density is lower in cases of low inlet gas flow rate. The oxygen conversion and oxygen partial pressure at the limited current density are about 0.66 and 17.0 kPa in case of the gas flow rate of 0.81 mL/s, and 0.312 and 27.3 kPa in case of the gas flow rate of 2.69 mL/s, which indicated that the insufficient oxygen supply

causes the low oxygen partial pressure so that the oxygen mass transfer resistance increases near the limited current density.

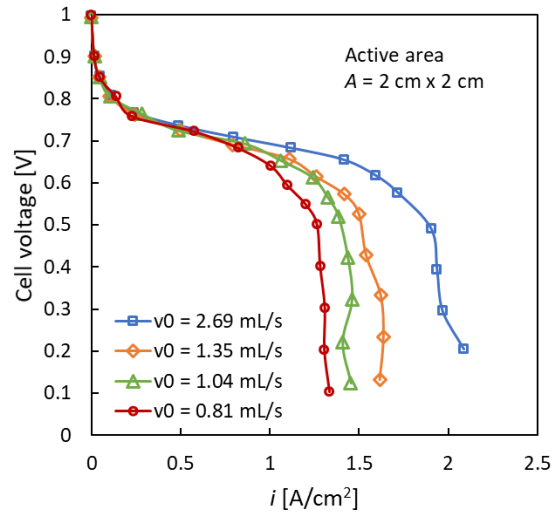


Figure 10. Polarization curves of different inlet gas flow rates (parallel gas channel)

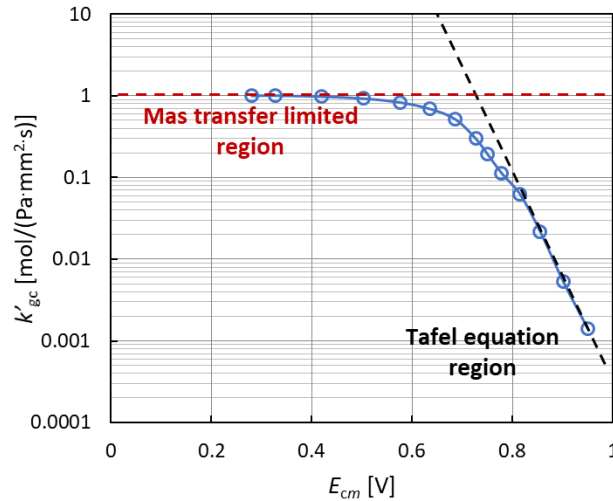


Figure 11. Kinetics data measured by differential reactor
(Gas channel: serpentine, humidified temperature: 75 °C, H₂ flow rate: 600 cm³/min (20 °C, 1 atm), O₂ flow rate: 300 cm³/min (20 °C, 1 atm))

To measure the kinetics data of the ORR, the polarization curve of MEA with the equal Pt-loading and catalyst layer thickness was measured under the high flow rate, where the oxygen conversion was 0.10 at 0.64 V of the IR-corrected cell voltage. Since the conversion is low, the cell can be regarded as a differential reactor, whose design equation can be written as Eq. [14], where k'_{gc} represents the partial-pressure-based apparent kinetics constant [mol/(Pa·m²·s)] at RH = 1, and \bar{x}_O represent the average oxygen conversion throughout the gas channel. Consequently, the observed ORR kinetics which contain the effectiveness factors can be calculated simply, as shown in Figure 11.

$$\frac{x_O}{A/v_0} = k'_{gc} \frac{RTP}{p_S^{sat}} \frac{(1 - \bar{x}_O)(y_{S0} + 2y_{O0}\bar{x}_O)}{(1 + y_{O0}\bar{x}_O)^2} \quad [14]$$

By applying the combined PFR followed by CSTR model to parallel gas channels, and the ORR kinetics measured by experiments, the performance of the cell voltage can be calculated by Eqs. [10] and [11]. Figure 12(a) and (b) shows the oxygen conversion under different ratios of active area to the inlet gas volume flow rate, which is regarded as the space time. Since the ORR has a similar behavior to the self-catalytic reaction, the oxygen conversion, which is proportional to the current density, of CSTR is higher than that of PFR at little space time, and lower than PFR at high space time. In case of low IR-corrected cell voltage, the critical space time, at which the CSTR and the PFR have the same performance, is longer than that in case of high IR-corrected cell voltage. However, the difference of the CSTR and PFR is not obvious at short space time. The compartment model has an intermediate performance between PFR and CSTR, and is close to the CSTR at long space time, which indicates the gas mixing in the parallel channel is more obvious at long space time.

On the other hand, the CSTR followed by PFR model, which is considered to characterize the serpentine channel, is closer to the PFR model. The calculation results indicate that the serpentine has better performance than the parallel at high oxygen conversion, since the effect of oxygen consumption is greater than water humidification, so that the gas mixing is not beneficial here.

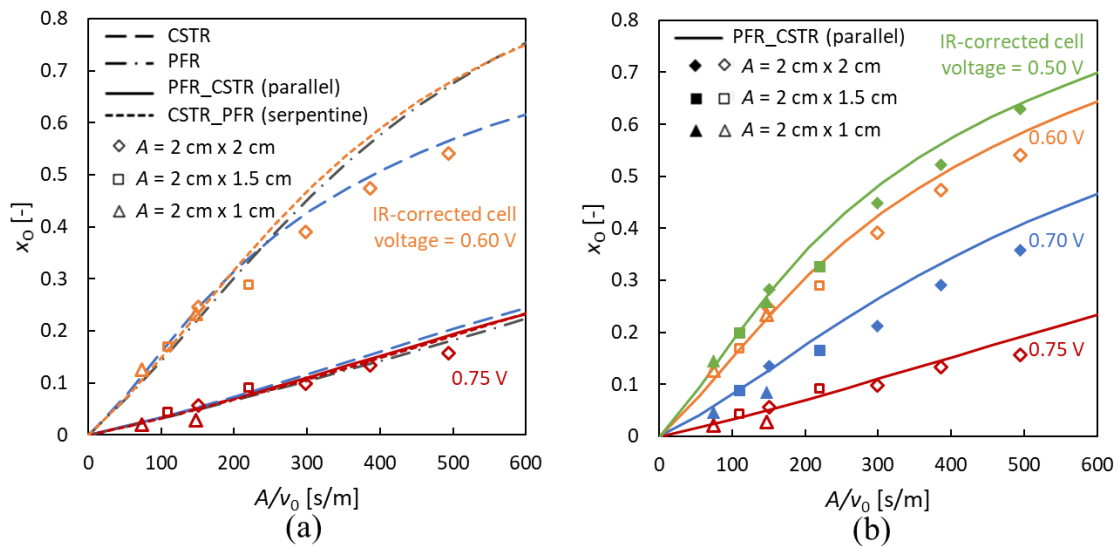


Figure 12. Relationship of oxygen conversion and space time at constant IR-corrected cell voltage (points: experimental results of parallel channels, curves: calculated results (a) CSTR, PFR, compartment models, (b) PFR_CSTR model)

Figure 12(b) shows the experimental data in case of parallel channel with calculated curve by the compartment model. The compartment model fits well with the experiment results at short space time. At long space time, the predicted oxygen conversion is higher than the experimental results. The reason may be that when calculating the ORR kinetics at high oxygen conversion, the reaction rate occurs near the outlet of the gas channel is higher due to the self-catalytic behavior, and the average conversion may be lower than the arithmetic mean of the conversion, so that the kinetics data may be overestimated.

In addition, in this study, the RTD is simulated without the reaction. However, since the gas composition changes due to the reaction, the total molar flow rate cannot be considered as a constant, especially when the oxygen conversion is high, and the real

RTD may diverge from the simulated results in this study. Furthermore, the temperature and total pressure distributions are also not negligible at high oxygen conversion. In a word, the compartment model needs to be modified at high conversion.

Conclusions

The method in the perspective of chemical engineering was applied to evaluate the PEFC, which can be regarded as a continuous reactor which has the gas mixing behavior between PFR and CSTR. To characterize the gas mixing behavior, the RTDs of parallel and serpentine gas channels were simulated by numerical method. The cross-flow of the serpentine channels is much more remarkable than that of parallel channel, since the pressure gradient between the neighbor channels is steep in case of the serpentine. The ununiform velocity distribution in the parallel channels, that is the gas has high velocity in the channels near the inlet and outlets, was confirmed. As the results, some gas with long residence time mixes with the gas with short residence time near the gas outlet, so that the PFR followed with CSTR model can be considered. On the other hand, the serpentine has obvious cross-flow where the pressure gradient is steep, *vice versa*, the CSTR followed by PFR model can be considered.

The polarization curves of different ratios of the active area to the gas inlet flow rate, which can be regarded as the space time, were measured experimentally with the parallel gas channel. Lower oxygen conversion obtained in the narrower active area and higher flow rate, i.e. shorter space time, at the identical IR-corrected cell voltage. The phenomenon indicates that the ORR has a similar behavior to the self-catalytic reaction, which is affected by the water humidification and oxygen consumption simultaneously.

According to the calculation results, the serpentine channel has better performance than the parallel channels at long space time, when the IR-corrected cell voltages are fixed. The reason is that the serpentine has similar performance to the PFR, and the effect of oxygen consumption is greater than water humidification, which means the gas mixing is not beneficial at long space time.

The compartment model of PFR followed by CSTR, which is expected to characterize the cell performance with the parallel channel, reproduces the experiment results well at short space time or low oxygen conversion. In the future, more accurate kinetics data and model should be used, and the effects of the ununiform distribution of temperature and total pressure should also be concerned to eliminate the deviation of the model from the experimental results. The method mentioned in this study can be applied to other shapes of gas channels to understand the gas macromixing, and may be helpful for the cell design.

Acknowledgments

This work was supported by the FC Platform Program: Development of design-for-purpose numerical simulators for attaining long life and high performance project (FY 2020–FY 2022) conducted by the New Energy and Industrial Technology Development Organization (NEDO), Japan.

References

1. Y. Qi, X. Li, S. Li, T. Li, M. Espinoza-Andaluz, P. Tunestål, and M. Andersson, *Int. J. Energy Res.*, **44**, 4352–4365 (2020).
2. F. Akitomo, T. Sasabe, T. Yoshida, H. Naito, K. Kawamura, and S. Hirai, *J. Pow. Sour.*, **431**, 205–209 (2019).
3. K. Takanohashi, T. Suga, M. Uchida, T. Ueda, Y. Nagumo, J. Inukai, H. Nishide, and M. Watanabe, *J. Pow. Sour.*, **343**, 135–141 (2017).
4. H. Nakajima, and K. Matsutani, *ECS Trans.*, **64**(3), 763–769 (2014).
5. M. Kawase, M. Nagayoshi, G. Inoue, and M. Kageyama, *ISCRE 23 & APCRE 7, Bangkok*, Sep. 8, OE03 (2014).
6. A. Nishimura, K. Yamamoto, T. Okado, Y. Kojima, M. Hirota, and M. L. Kolhe. *Energy*, **205**, 117875 (2020).
7. A. Nishimura, K. Shibuya, A. Morimoto, S. Tanaka, M. Hirota, Y. Nakamura, M. Kijima, and M. Narita, *J. Environ. Eng.*, **6**, 1–16 (2011).
8. F. Liu, M. Kvesić, K. Wippermann, U. Reimer, and W. Lehnert, *J. Electrochem. Soc.*, **160**, F892 (2013).
9. A.A. Kulikovskiy, *Electrochim. Acta*, **49**, 617–625(2004).
10. G. Inoue, T. Yoshimoto, Y. Matsukuma. M. Minemoto, H. Itoh, and S. Tsurumaki, *J. Pow. Sour.*, **162**, 94–104 (2006).
11. J. Park and X. Li, *Int. J. Energy Res.* **35**, 583–593 (2011).
12. K. Nishida, R. Nakauchi, Y. Maeda, T. Umekawa, and M. Kawasaki, *ECS Trans.*, **80** (8) 527–534 (2017).
13. C. Chan, N. Zamel, X. Li, and J. Shen, *Electrochim. Acta*, **65**(30), 13–21 (2012).
14. Y. Kakizawa, T. Kobayashi, M. Uchida, T. Ohno, T. Suga, M. Teranishi, M. Oneda, T. Saiki, H. Nishide, M. Watanabe, A. Iiyama, and J. Inukai, *J. Surf. Finish. Soc. Jpn.*, **72**, 230–237 (2021).
15. W. K. Epting and S. Litster, *Int. J. Heat Mass Transf.*, **306**, 674–684 (2016).
16. O. Panchenko, E. Borgardt, W. Zwaygardt, F. J. Hackemüller, M. Bram, N. Kardjilov, T. Arlt, I. Manke, M. Müller, D. Stolten, and W. Lehnert, *J. Pow. Sour.*, **390**, 108–115 (2018).
17. K. Nishida, R. Funaok, T. Furukawa, and Y. Kono, *ECS Trans.*, **98** (9) 89–96 (2020).
18. T. Berning, N. Djilali, and *J. Electrochem. Soc.*, **150**, 1589–1598 (2003).
19. S. Zhang, S. B. Beale, U. Reimer, M. Andersson, and W. Lehnert, *Int. J. Hydrog. Energy*, **45**, 19761–19777 (2020).
20. P. D. Neufeld, A. R. Janzen, and R. A. Aziz, *J. Chem. Phys.*, **57**, 1100 (1972)
21. C. R. Wilke, *J. Chem. Phys.*, **18**, 517 (1950)
22. J. T. Gostick, M.W. Fowler, M. D. Pritzker, M. A. Ioannidis, and L. M. Behra, *J. Pow. Sour.*, **162**, 228–238 (2006).
23. M. Kawase, K. Yamaguchi, M. Kageyama, K. Sato, and G. Inoue, *ECS Trans.*, **75**(14), 147–156(2016).
24. M. Kawase, K. Sato, R. Mitsui, H. Asonuma, M. Kageyama, K. Yamaguchi, and G. Inoue, *AIChE J.* **63**, 249–256 (2017).
25. S. Cruz-Manzo and R. Chen, *J. Electroanal. Chem.*, **694**, 45–55 (2013).